Clays and Clay Minerals, Vol. 64, No. 3, 230–244, 2016.

INFLUENCE OF AQUEOUS Si AND Fe SPECIATION ON TETRAHEDRAL Fe(III) SUBSTITUTIONS IN NONTRONITES: A CLAY SYNTHESIS APPROACH

FABIEN BARON*, SABINE PETIT, EMMANUEL TERTRE, AND ALAIN DECARREAU

Institut de Chimie des Milieux et Matériaux de Poitiers, IC2MP UMR 7285, Université de Poitiers, CNRS, 86073 Poitiers, France

Abstract—Most dioctahedral 2:1 swelling clays in natural systems contain ferric iron, Fe(III), which can be located in both the tetrahedral and the octahedral sheets. The distribution of Fe(III) between octahedral and tetrahedral sites in nontronite depends on the Fe and Si speciation during nontronite synthesis. The role played by the chemical properties of solutions in the Fe(III) distribution between structural sites was studied through nontronite syntheses. A chemical series of Fe(III)-nontronites with variable tetrahedral $^{[4]}$Fe(III) content (x) ($[Si_{4-x}Fe(III)_x]Fe(III)_2O_{10}(OH)_2Na_x$) was synthesized at 150ºC across a range of initial aqueous pH values between 11 and 14. The permanent layer charge, due to Fe(III)-for-Si(IV) tetrahedral substitutions only, ranged from 0.43 to as high as 1.54 per half-unit cell. A $d_{06\bar{3}3}$ value of 1.562 Å was measured by X-ray diffraction (XRD) for the highest charged nontronite (x = 1.54). This high $d_{06\bar{3}3}$ value has not been reported in the literature for a dioctahedral smectite until now. The $^{[4]}$Fe(III) content (x) of the synthetic nontronites, estimated using Fourier-transform infrared spectroscopy (FTIR) through the wavenumber of the main stretching νSi−O band, was correlated with synthesis pH and its influence on calculated aqueous Si speciation. The increase in synthesis pH induced the increase in anionic aqueous Si species ratios (*i.e.* $H_3SiO_{4\,(aq)}^-$ and $H_2SiO_{4\,(aq)}^-$), and favored the incorporation of Fe(III) in tetrahedral sites of synthesized nontronites. During nontronite formation in natural systems, the level of tetrahedral Fe(III)-for-Si(IV) substitutions may, therefore, be partly linked to the aqueous Si speciation and thus strongly dependent on the pH of the crystallization fluids.

Key Words—Aqueous Speciation, Clay Minerals, Clay Synthesis, Fe(III), Infrared Spectroscopy, Iron, Nontronite, Permanent Charge, Smectite, Tetrahedral Substitution.

INTRODUCTION

The smectite group is composed of 2:1 trioctahedral and dioctahedral clay minerals, which can exhibit a wide chemical variability in their structure. For dioctahedral smectites, a continuous solid-solution (aluminum (Al(III))−ferric iron (Fe(III)) exists between the beidellite (Al(III)) and nontronite (Fe(III)) end-members (Andrieux and Petit, 2010; Petit *et al.*, 2015). Fe(III)-rich dioctahedral smectites are ubiquitous at the Earth's surface and exhibit a large variability in terms of chemistry and charge in both tetrahedral and octahedral sheets. The common octahedral cations in natural dioctahedral smectite are Al(III), Fe(III), and magnesium (Mg(II)), whereas Al(III), and sometimes Fe(III), can substitute for silicon (Si(IV)) in the tetrahedral sheet (Decarreau and Petit, 2014). The identification of nontronite on the surface of Mars from infrared spectroscopic investigations (Poulet *et al.*, 2005) stimulated interest in the conditions of the formation and suitable spectroscopic fingerprints of this Fe(III)-rich clay mineral (*e.g.* Poulet *et al.*, 2009). These Fe(III)-rich smectites are also interesting as precursors for the syntheses of materials used in many applications such as catalysis (*e.g.* Zen *et al.*, 1996; Liu *et al.*, 2014; Li *et al.*, 2015), the adsorption of dyes or pollutants (*e.g.* Gupta *et al.*, 2006), the degradation of organic compounds (*e.g.* Hofstetter *et al.*, 2006; Neumann *et al.*, 2009), and the reduction of the mobility of heavy metals (*e.g.* Jaisi *et al.*, 2009; Yang *et al.*, 2012; Ilgen *et al.*, 2012). Moreover, pure Fe(III)-nontronites with a large amount of Fe(III)-for-Si(IV) substitutions can be useful for studying the specific role of tetrahedral Fe(III) ($^{[4]}$Fe(III)) in smectite reactivity, especially for redox studies (Neumann *et al.*, 2011), and can also be used as reference minerals for spectroscopic techniques.

Due to the Fe(III)/Al(III) partitioning between tetrahedral and octahedral sites in dioctahedral smectites and the strong preference of Al(III)-for-Si(IV) substitutions in the tetrahedral sheet (Decarreau and Petit, 2014), natural smectites with very high Fe(III)-for-Si(IV) tetrahedral substitutions are uncommon. Nevertheless, tetrahedral Fe(III)-for-Si(IV) substitutions are found in natural dioctahedral smectites (Goodman *et al.*, 1976; Gates *et al.*, 2002; Gates, 2005). Because natural nontronites with large $^{[4]}$Fe(III) content are rare, laboratory synthesis is a useful method for studying Fe(III) structural distribution. Syntheses of nontronite using different protocols to obtain the beidellite–nontronite series have been well documented (Petit *et al.*, 1995; Andrieux and Petit, 2010), the saponite (Mg-rich trioctahedral smectite)–nontronite series (Grauby *et*

* E-mail address of corresponding author:
fabien.baron@univ-poitiers.fr
DOI: 10.1346/CCMN.2016.0640309

al., 1994), or pure Fe(III)-nontronites (free of Al(III) and Mg(II); Decarreau *et al.*, 2008) have been well documented. Clay synthesis is essential for obtaining dioctahedral smectites free of Al(III) and Mg(II) and with a controlled amount of Fe(III)-for-Si(IV) substitutions. However, the synthesis of these dioctahedral smectites free from Mg(II) requires specific pH conditions (Decarreau *et al.*, 2008; Andrieux and Petit, 2010; Petit *et al.*, 2015).

In this study, a characterization of both the synthetic Fe(III)-nontronite and the solutions recovered at the end of the syntheses was performed to understand the relation between aqueous speciation and the crystal-chemistry of synthetic Fe(III)-nontronites with Fe(III)-for-Si(IV) substitutions. For this purpose, an Fe(III)-nontronite series $[Si_{4-x}Fe(III)_x]Fe(III)_2O_{10}(OH)_2Na_x$ with a wide range of permanent layer charge produced by Fe(III)-for-Si(IV) substitutions in the tetrahedral sheets was synthesized.

EXPERIMENTAL

Fe(III)-nontronites were synthesized according to the procedure described by Decarreau *et al.* (2008) using a co-precipitated starting gel obtained as follows:

$$2\ SiNa_2O_3 + Fe(II)Cl_2 \rightarrow Si_2Fe(II)Na_2O_6 + 2\ NaCl \quad (1)$$

The pH of the suspension during co-precipitation was 12.55 at 25ºC. After precipitation, the starting gel was collected by filtration and washed lightly with Milli-Q® pure water (18 MΩ cm) during the filtration process. The starting gel was then oxidized during drying at 60ºC before being crushed. Then, 500 mg of the powdered starting gel was placed in contact with 30 mL of NaOH solution at fixed pH (pH_s) ranging from 11 to 14 at 25ºC (Table 1) in Teflon® metallic-coated hydrothermal reactors (Parr®, reactor number: 4744). The solutions were obtained from various dilutions of Normadose 1 M (NaOH).

Syntheses of Fe(III)-nontronites were performed at 150ºC under equilibrium vapor pressure for 6 days. The temperature was chosen to obtain better crystallinity of the synthesized nontronites without crystallization of aegirine, according to Decarreau *et al.* (2004, 2008). The synthesized solid phase was removed from the suspension at the end of the synthesis by filtration (<0.1 μm) and was dried at 50ºC.

The pH of the starting solutions (pH_s) and of the solutions at the end of synthesis (pH_f) was measured at 25ºC using a FiveEasy™ Mettler Toledo pH meter (pH ± 0.04) calibrated with three buffer solutions at pH 7.01, 10.14, and 12.00.

Total aqueous Si was measured according to the methylene blue method from Strickland and Parsons (1972) using a Jenway 6300 spectrophotometer at 820 nm. For analysis, solutions recovered at the end of the synthesis were diluted in Milli-Q® pure water (18 MΩ cm) to measure the aqueous concentrations in the linear range of the calibration curve (*i.e.* from 1.78×10^{-5} to 1.78×10^{-4} mol L^{-1}).

Total aqueous sodium (Na) and Fe in filtrated <0.1 μm solutions were measured by atomic absorption spectroscopy (AAS) using a Varian® AA240FS spectrometer. To take into account matrix matching, solutions recovered at the end of the synthesis were diluted in 2 wt.% HNO_3 to measure aqueous concentrations in the linear range of the calibration curve (*i.e.* from 8.26×10^{-6} to 4.35×10^{-5} mol L^{-1} for Na; from

Table 1. Chemical properties of solutions of the 16 syntheses: pH of the starting solutions (pH_s), and pH at the end of syntheses (pH_f).

Sample	pH_s	pH_f	Si (mol L^{-1})	Na (mol L^{-1})
NT 25	14*	13.70	5.19×10^{-2}	9.64×10^{-1}
NT 19	13.60	13.41	4.81×10^{-2}	6.06×10^{-1}
NT 18	13.44	13.21	4.71×10^{-2}	3.65×10^{-1}
NT 7	13.30	13.20	4.31×10^{-2}	2.60×10^{-1}
NT 6	13.16	13.08	3.82×10^{-2}	1.76×10^{-1}
NT 5	13.02	12.86	3.20×10^{-2}	1.18×10^{-1}
NT 4	12.87	12.67	2.96×10^{-2}	8.65×10^{-2}
NT 3	12.69	12.33	2.39×10^{-2}	5.88×10^{-2}
NT 2	12.45	12.04	2.10×10^{-2}	4.39×10^{-2}
NT 1	12.27	11.79	1.71×10^{-2}	3.55×10^{-2}
NT 0	12.03	11.44	1.47×10^{-2}	3.09×10^{-2}
NT 24	11.97	11.00	1.31×10^{-2}	2.50×10^{-2}
NT 23	11.75	10.73	1.29×10^{-2}	2.52×10^{-2}
NT 22	11.54	10.66	1.18×10^{-2}	2.33×10^{-2}
NT 21	11.38	10.46	1.25×10^{-2}	2.16×10^{-2}
NT 20	11.12	10.54	1.09×10^{-2}	2.13×10^{-2}

* corresponds to Normadose 1 M NaOH solution.
Total aqueous Si and Na concentrations (mol L^{-1}) measured at the end of each synthesis.

https://doi.org/10.1346/CCMN.2016.0640309 Published online by Cambridge University Press

8.95×10^{-6} to 1.79×10^{-4} mol L^{-1} for Fe). Moreover, analyzed samples were prepared in KNO_3 solution at a final concentration of 0.05 mol L^{-1} to take into account the possible Na ionization in the flame during measurements.

Synthetic samples were Ca saturated to simplify the interpretation of the chemistry of the solid samples. Six contacts of at least 12 h between 70 mg of the synthetic sample and 5 mL of a 1 M $CaCl_2$ solution were performed. The synthetic samples were washed by centrifugation using Milli-Q® pure water (18 MΩ cm) to remove excess salt, and a silver chloride test was used to check the efficiency of the procedure.

Chemical analysis was performed on washed solid samples from carbon-coated powder-pressed pellets (5 mm in diameter and approximately 1 mm thick) using a JEOL 5600 LV Scanning Electron Microscope (SEM) equipped with an Energy Dispersive Spectrometer (EDS). Chemical analyses were performed in backscattering electron mode with an accelerating voltage of 15 kV, a current of 1 nA, a counting time of 60 s, and a working distance of 16.5 mm. Albite (Na, Si), almandine (Fe), and diopside (Ca) were used as standards. The chemical analyses (Table 2) were expressed in atomic percent of elements (at.%).

The powder XRD patterns were recorded using a Bruker D8 advance diffractometer (CuKα radiation, 40 kV and 40 mA) with a step size of 0.025º2θ over the 2−65º2θ range and a counting time of 0.6 s. The recording of the 57−63º2θ range for the $06\bar{3}3$ reflection ($d_{06\bar{3}3}$) was performed with a step size of 0.025º2θ and a counting time of 4 s. The XRD patterns of oriented preparations of the synthesized samples, after Ca saturation, in the air-dried (AD) condition, and after the ethylene-glycol (EG) solvation, were obtained using a step size of 0.025º2θ over the 2−35º2θ range and a counting time of 0.6 s as acquisition conditions.

FTIR spectra were obtained in transmission mode at 4 cm^{-1} resolution in the middle infrared (MIR) range (4000−400 cm^{-1}) using a Magna-IR 760 Nicolet spectrometer equipped with an Ever-Glo source, a KBr beam splitter, and a DTGS-KBr detector. MIR spectra were collected from KBr pellets (obtained by mixing 1 mg of sample with 150 mg of KBr) that were dried for 1 day at 110ºC. Near infrared (NIR) spectra were measured from powdered samples with a ThermoScientific Nicolet 6700 spectrometer (with a white light source and a CaF_2 beam splitter) equipped with a ThermoScientific Integrating Sphere (diffuse reflectance) over the 7500−3850 cm^{-1} range and using 4 cm^{-1} resolution.

Transmission electron microscopy (TEM) and high-resolution TEM (HRTEM) observations were performed using a JEOL 2100 UHR (LaB_6) transmission electron microscope at 200 kV. Samples for examination by TEM and HRTEM were dispersed in ethanol using sonication and then, a droplet of the dispersion was placed and dried on a TEM copper grid.

RESULTS

Chemical analyses

Aqueous data. The pH at the end of syntheses (pH_f) decreased significantly from the pH of the starting solutions (pH_s) (Table 1). This trend reflected the consumption of OH^- groups by the crystallization of hydroxylated 2:1 layers. The filtered solutions at the end of syntheses for all experiments were clear. The total aqueous Fe concentrations measured for all samples were two orders of magnitude lower than those measured for Si and Na, with a value equal to ~10^{-4} mol L^{-1} for all samples (individual data not shown in Table 1). The total aqueous Si and Na concentrations (Table 1) increased with increase in pH. Nevertheless, the total aqueous Na concentrations were always significantly higher than the total aqueous Si concentrations (Table 1).

Solid data. The chemical analysis of the starting gel indicated an Fe/Si ratio of 0.74, corresponding to x = 0.55 in the $[Si_{4-x}Fe(III)_x]Fe(III)_2O_{10}(OH)_2Na_x$ half-unit cell (Table 2). This value, which was greater than the theoretical Fe/Si ratio of 0.5 (x = 0) used for the preparation of the starting gel, could be due to the high solubility of Si at pH as high as 12.55 during the co-precipitation of the starting gel.

Table 2. Chemical analysis (SEM-EDX) (at.%) of the starting gel and of the samples synthesized (NT25, NT18, NT6, NT3, NT0, NT22, and NT20) after Ca saturation.

Sample	O	Si	Fe	Ca	Na	Fe/Si
NT 25	57.12	15.21	21.83	3.58	2.06	1.43
NT 18	57.69	15.92	21.74	3.11	1.27	1.37
NT 6	58.77	17.91	19.59	2.64	0.81	1.09
NT 3	59.74	19.50	17.90	2.50	0.16	0.92
NT 0	60.98	22.00	14.99	1.48	0.23	0.68
NT 22	60.87	21.75	15.10	1.75	0.20	0.69
NT 20	60.76	21.53	15.51	1.84	0.12	0.72
Starting gel	57.29	19.25	14.26	–	8.16	0.74

https://doi.org/10.1346/CCMN.2016.0640309 Published online by Cambridge University Press

Iron in the synthesized samples was trivalent (Fe(III)), as reported previously by Decarreau *et al.* (2008) for a nontronite synthesized in the same conditions (150ºC, pH_f = 12.5). Chemical analyses were performed on seven representative samples after Ca saturation (Table 2). With the increase in pH_f, the Fe(III) content in synthesized samples increased, whereas the Si content decreased (Table 2). Despite the caution in the Ca saturation of synthetic samples, Na was not totally exchanged by Ca, especially for samples with a large $^{[4]}$Fe(III) content (NT6, NT18, and, NT25; Table 2). For the NT20, NT22, and NT0 samples, the Fe/Si ratios were similar to the Fe/Si ratio of the starting gel (Tables 1, 2). For the NT3, NT6, NT18, and NT25 samples, the Fe/Si ratios increased when pH_f increased.

The formulae of the half-unit cell of synthetic nontronites (Table 3) were calculated from the Fe/Si ratio (Table 2). The amount of octahedral $^{[6]}$Fe(III) was fixed at 2, which corresponds to a full theoretical dioctahedral occupancy in this chemical series. The $^{[4]}$Fe(III) content was obtained from the subtraction of total Fe(III) by $^{[6]}$Fe(III) (Table 3). The large uncertainty in the quantification of the amount of Na prevented an accurate determination of the value of the interlayer charge. Nevertheless, the amount of Ca(II) and Na(I) (Table 3) corresponded to a rough estimate of the layer charge and the negative tetrahedral charge (x) was relatively well compensated by the amount of interlayer cations (Ca(II) and Na(I), Table 3). For the NT3, NT6, NT18, and NT25 samples, the $^{[4]}$Fe(III) content (x) increased with the increase in pH_f.

XRD data

The powder XRD patterns of the synthetic samples exhibited reflections at 12.21 Å (001), 4.61 Å ($02\bar{1}1$), 3.05 Å (004), 2.63 Å ($13\bar{2}0$), and 1.528–1.562 Å ($06\bar{3}3$) (Figure 1), corresponding to a Na-nontronite (Brindley and Brown, 1980; Decarreau *et al.*, 2008). No other crystalline phases were detected in the synthetic nontronite samples. The apparent d_{001} distance at 12.21 Å indicated that most of the layers were in a monohydrated state (*e.g.* Brindley and Brown, 1980; Suquet *et al.*, 1987; Ferrage *et al.*, 2007). The 001 reflections broadened progressively with decreases in the $^{[4]}$Fe(III) content. The $d_{06\bar{3}3}$ was correlated with the total Fe(III) content in smectite samples (Eggleton, 1977; Brigatti, 1983; Köster *et al.*, 1999; Heuser *et al.*, 2013; Petit *et al.*, 2015). The shift of the $d_{06\bar{3}3}$ from 1.529 to 1.562 Å corresponded to an increase in total Fe(III) content in synthesized nontronites and thus to an increase in the $^{[4]}$Fe(III) content (Figure 1b). Even if the samples were relatively poorly crystalline, the diffracted intensities for all nontronite samples at ~30º2θ were close to the baseline and suggested a lack of amorphous solid materials (amorphous solid material creates an elevation of the overall diffraction intensity above the baseline of ~30º2θ).

After Ca saturation in air-dry (AD) conditions (Figure 2), the d_{001} was observed near 14 Å for the synthesized nontronite with the smallest $^{[4]}$Fe(III) content, and shifted progressively toward 12.1 Å for the synthesized nontronite with the largest $^{[4]}$Fe(III)

Table 3. Half-unit cell of synthesized nontronites $[Si_{4-x}Fe(III)_x]Fe(III)_2O_{10}(OH)_2M(I)_x$ after Ca saturation determined from chemical analysis (see text for details). The layer charge (x) is estimated from the amount of substitutions in the tetrahedral sheet for the samples (NT25, NT18, NT6, NT3, NT0, NT22, and NT20). For values in *italics*, the layer charge (x) was calculated according to the FTIR data from equation 2 (see text for details). The errors in the measurement of the wavenumber of the νSi–O vibration and the $d_{06\bar{3}3}$ value are 0.5 cm^{-1} and 0.003 Å, respectively.

Sample	Si(IV)	$^{[4]}$Fe(III)	$^{[6]}$Fe(III)	Ca(II)	Na(I)	Interlayer cations	x (layer charge)	ν Si–O (cm^{-1})	$d_{06\bar{3}3}$ (Å)
NT 25	2.46	1.54	2.00	0.58	0.33	1.49	1.54	949	1.562
NT 19							*1.50*	955	1.556
NT 18	2.54	1.46	2.00	0.50	0.20	1.19	1.46	957	1.554
NT 7							*1.30*	965	1.547
NT 6	2.87	1.13	2.00	0.42	0.13	0.97	1.13	977	1.541
NT 5							*0.99*	982	1.540
NT 4							*0.85*	990	1.536
NT 3	3.13	0.87	2.00	0.40	0.03	0.83	0.87	993	1.537
NT 2							*0.68*	999	1.533
NT 1							*0.57*	1005	1.533
NT 0	3.57	0.43	2.00	0.24	0.04	0.52	0.43	1009	1.529
NT 24							*0.53*	1007	1.531
NT 23							*0.49*	1009	1.530
NT 22	3.54	0.46	2.00	0.29	0.03	0.60	0.46	1010	1.528
NT 21							*0.50*	1009	1.531
NT 20	3.49	0.51	2.00	0.30	0.02	0.62	0.51	1009	1.530

https://doi.org/10.1346/CCMN.2016.0640309 Published online by Cambridge University Press

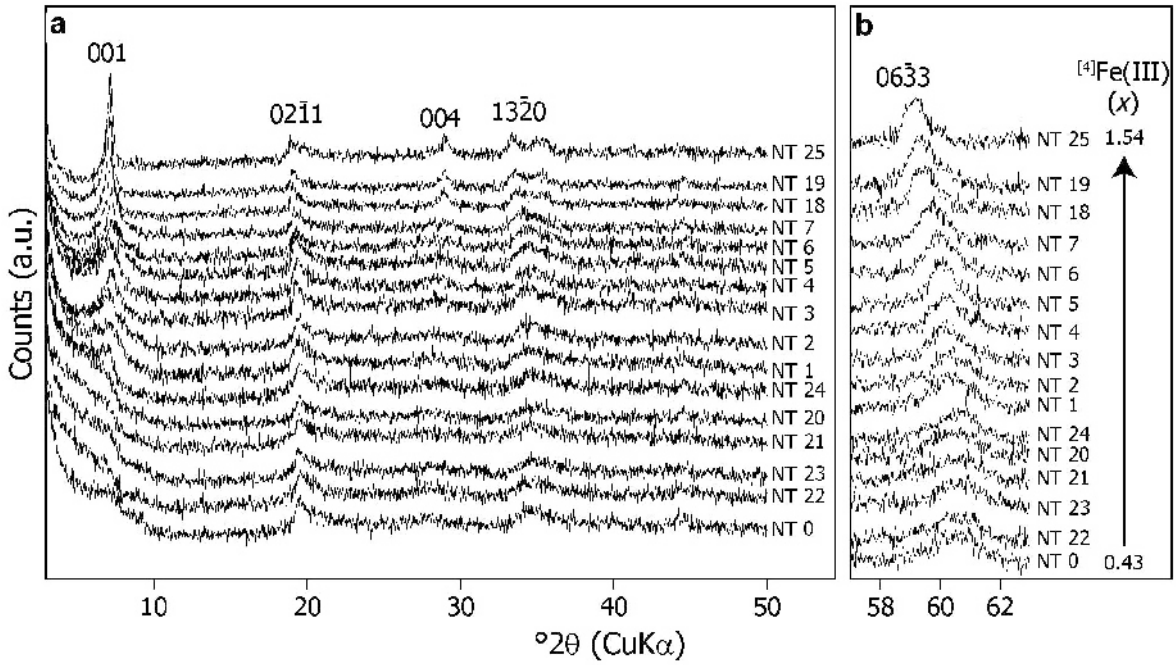

Figure 1. Powder XRD patterns of the synthesized samples (NT25, NT19, NT18, NT7, NT6, NT5, NT4, NT3, NT2, NT1, NT24, NT20, NT21, NT23, NT22, and NT0). The $^{[4]}$Fe(III) content (x) of the synthesized samples $[Si_{4-x}Fe(III)_x]Fe(III)_2O_{10}(OH)_2Na_x$ increases from the bottom to the top.

content. For all Ca-saturated samples, the d_{001} corresponded to mixed layers between the bi-hydrated state layers (d_{001} = 14.9−15.7 Å) and mono-hydrated state layers (d_{001} = 11.6−12.9 Å). Even for the sample characterized by the largest amount of $^{[4]}$Fe(III) (NT25), a d_{001} value of 12.1 Å indicated that most of the Ca(II) and Na(I) interlayer cations are in the mono-hydrated state. The continuous shift of the 001 reflection from 14 Å to 12.1 Å was due to the increase in layer charge (here Fe(III)-for-Si(IV) substitutions only), which influences the hydration properties of the samples (Sato *et al.*, 1992; Michot *et al.*, 2005; Ferrage *et al.*, 2007, 2010).

After Ca saturation and ethylene-glycol (EG) solvation (Figure 2), the XRD patterns of the nontronite with the smallest $^{[4]}$Fe(III) content exhibited a d_{001} value of 16.9 Å, which corresponds to two layers of EG molecules (MacEwan, 1948; Reynolds, 1965; Chassin, 1972; Suquet *et al.*, 1977). The d_{001} shifted progressively from 16.9 to 14.9 Å for the nontronite with the largest $^{[4]}$Fe(III) content, corresponding to mixed-layers of one and two layers of the EG complex, as observed previously by Decarreau *et al.* (2008) for a nontronite ($^{[4]}$Fe(III) (x) = 0.75) synthesized under similar conditions. Smectite layers with a d_{001} value close to 14−15 Å after EG solvation were reported in the literature for very high-charge Ca-saturated smectites ($\geqslant$1.0 layer charge per half-unit cell) (Suquet *et al.*, 1977; Sato *et al.*, 1992). A d_{001} value of 14.9 Å was observed for the NT25 nontronite having the greatest degree of Fe(III)-for-Si(IV) substitutions, revealing a large proportion of layers with one layer of EG molecules (the d_{001} value of a 2:1 layer with one EG layer is 14.3 Å: MacEwan, 1948; Brindley, 1966).

Despite the caution taken during the preparation of oriented samples, the nontronite samples were not well oriented due to their small particle size. For these reasons, only the d_{001} and the d_{004} were observed on the oriented XRD patterns, with some *hkl* reflections, which in turn prevented the calculation of XRD patterns or any quantitative assessments of the different layer types (dehydrated, mono-hydrated, bi-hydrated layers).

TEM data

Observations by TEM revealed that particles of synthetic nontronites formed foliated aggregates characteristic of smectites (Figure 3). The HRTEM images show that aggregated particles were crystallized with a layered structure (Figure 4). Amorphous solid materials were not identified in the samples studied.

FTIR data

OH-stretching region. For all synthesized samples, MIR spectra (Figure 5a) exhibited an absorption band at 3560 cm^{-1}, as previously observed for natural nontronites (Goodman *et al.*, 1976; Gates, 2005, 2008) and synthetic Fe(III)-rich smectites (Decarreau *et al.*, 2008; Andrieux and Petit, 2010; Petit *et al.*, 2015). This band was attributed to the stretching (ν) Fe_2^{3+}-OH mode and remained at the same position regardless of the sample.

https://doi.org/10.1346/CCMN.2016.0640309 Published online by Cambridge University Press

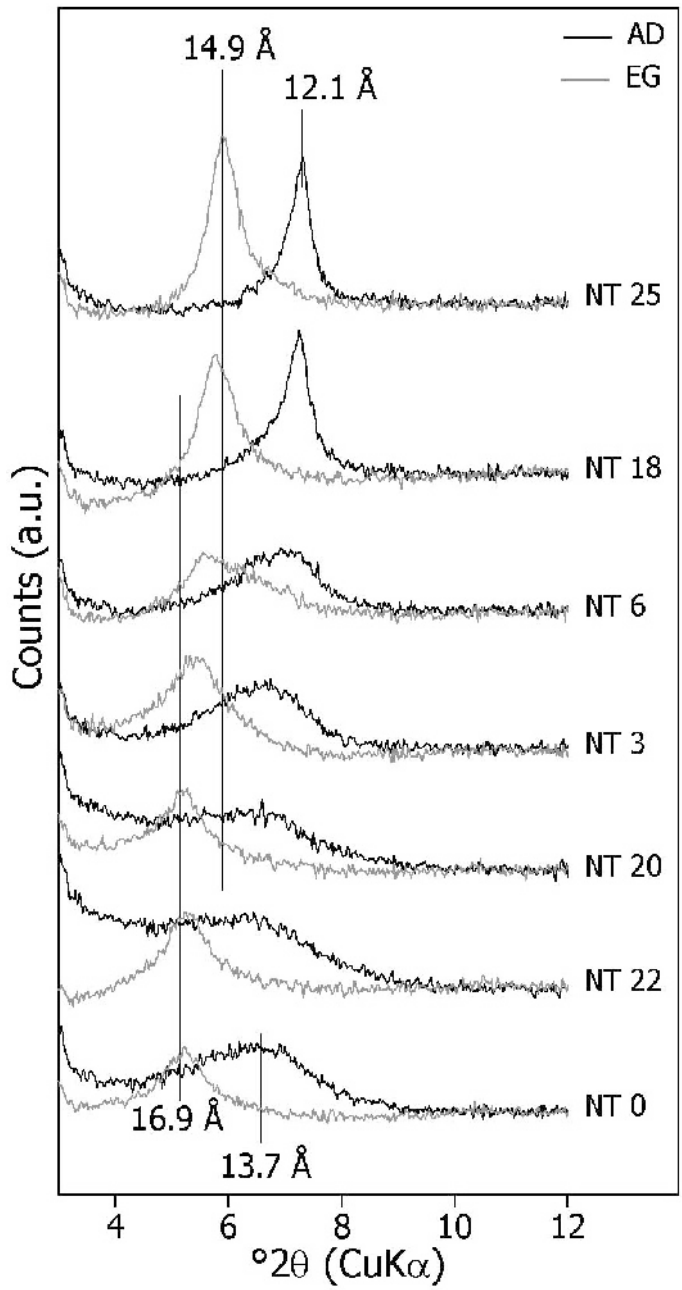

Figure 2. XRD patterns recorded for the oriented preparation of synthesized samples (NT25, NT18, NT6, NT3, NT20, NT22, and NT0) after Ca saturation. Patterns recorded in air-dry conditions (AD) and after ethylene-glycol solvation (EG) are represented by black lines and gray lines, respectively. The $^{[4]}$Fe(III) content (x) of the synthesized samples $[Si_{4-x}Fe(III)_x]Fe(III)_2O_{10}(OH)_2M(I)_x$ increases from the bottom to the top.

The νFe_2^{3+}-OH band confirmed the occurrence of Fe(III) only in a dioctahedral structure in the series.

Si–O stretching region. For natural nontronites, the νSi–O region consisted of the overlapping of components in the 1070–1110 cm^{-1} and 1034–1000 cm^{-1} ranges (Goodman *et al.*, 1976; Yan and Stucki, 1999, 2000; Fialips *et al.*, 2002). The νSi–O vibrations were affected only slightly by the amount of Fe(III) in the octahedral sheet (Gates, 2005; Petit *et al.*, 2015) but were very sensitive to the amount of Fe(III) in the tetrahedral sheets (Goodman *et al.*, 1976; Petit *et al.*, 2015). For a synthetic nontronite with $^{[4]}$Fe(III) (x) = 0.75 per half-unit cell, a νSi–O vibration at 991 cm^{-1} was observed by Decarreau *et al.* (2008). For the synthesized samples, the most intense νSi–O band

https://doi.org/10.1346/CCMN.2016.0640309 Published online by Cambridge University Press

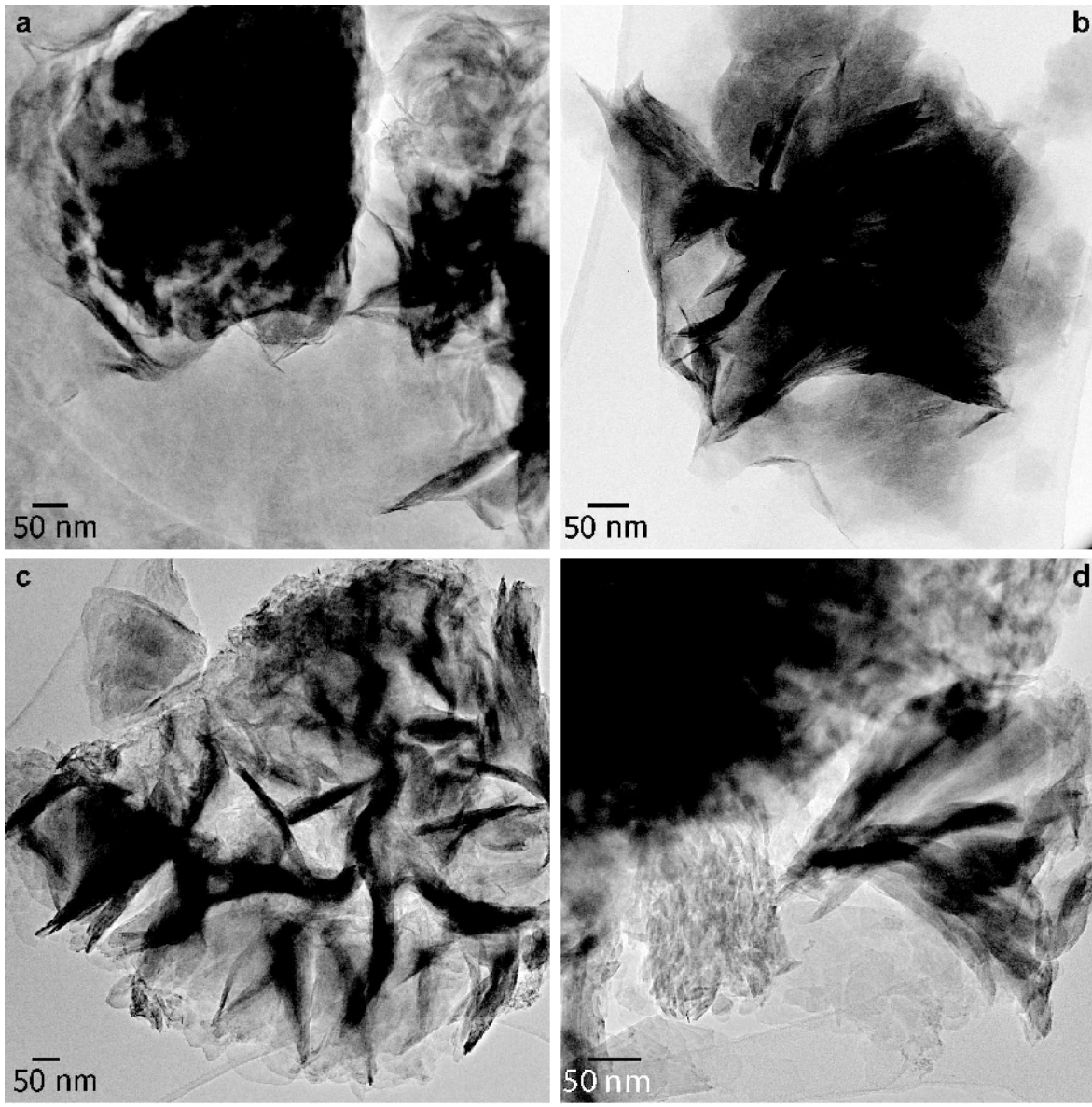

Figure 3. TEM images of synthesized samples NT0 (a), NT3 (b), NT6 (c), and NT18 (d). The images are representative of the synthesized samples overall. All aggregates are composed of crystalline clay particles.

(Figure 5b) shifted continuously from 1011 cm^{-1} to 950 cm^{-1} with an increase in $^{[4]}$Fe(III) (Figures 5b and 6a). The shift of the νSi–O band toward 950 cm^{-1}, corresponding to the lowest wavenumber found for this nontronite series (Figure 6a), was associated with an $^{[4]}$Fe(III) content of 1.54 per half-unit cell. A low wavenumber of 958 cm^{-1} for the νSi–O band was previously observed for a ferri-phlogopite ($[Si_3Fe(III)]Mg_3O_{10}(OH)_2K$) (Farmer, 1974).

In Figure 7, the $^{[4]}$Fe(III) content from the chemical analysis (Table 3) were plotted versus the wavenumber of the main νSi–O band observed for the synthesized samples. A linear relationship was observed in accordance with the following regression:

$$\nu Si{-}O\ (cm^{-1}) = -54.5 \times {}^{[4]}Fe(III) + 1037 \qquad (2)$$

OH-bending region. The spectra of synthetic samples with a small $^{[4]}$Fe(III) content were similar and were characterized by two absorption bands in the OH-bending (δOH) region at 816 and 840 cm^{-1} (Figures 5b and 6b), similar to natural nontronites (Goodman *et al.*, 1976; Madejovà *et al.*, 1996; Keeling *et al.*, 2000; Gates, 2005) and synthetic Fe(III)-rich smectites (Decarreau *et al.*, 2008; Andrieux and Petit, 2010; Petit *et al.*, 2015). The band at 816 cm^{-1} was attributed to the δFe_2^{3+}-OH vibrations (*e.g.* Farmer, 1974; Goodman *et al.*, 1976; Petit *et al.*, 1992; Gates, 2005; Decarreau *et al.*, 2008). For samples with low to

https://doi.org/10.1346/CCMN.2016.0640309 Published online by Cambridge University Press

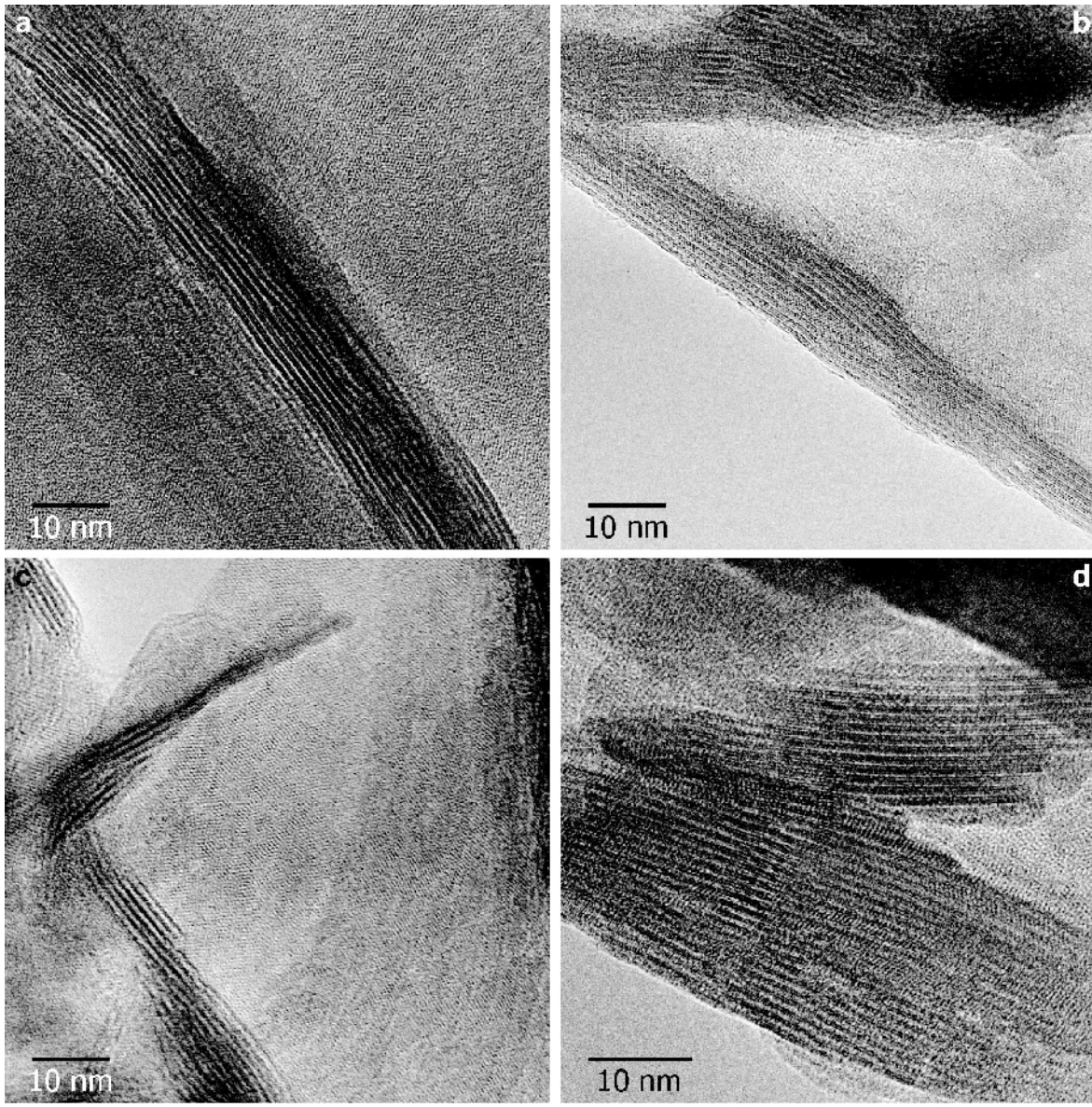

Figure 4. HRTEM images of synthesized samples NT0 (a), NT3 (b), NT6 (c), and NT18 (d). The images are representative of the synthesized samples overall.

intermediate $^{[4]}$Fe(III) content, the relative intensity of the 840 cm^{-1} absorption band did not significantly change compared to the 816 cm^{-1} band (Figure 6b) when the $^{[4]}$Fe(III) content increased. The 840 cm^{-1} band shifted to 855 cm^{-1} with an increase in the $^{[4]}$Fe(III) content. Many assumptions exist in the literature concerning the assignment of the band at 840–855 cm^{-1}, which is usually observed for nontronite (Petit *et al.*, 1992; Gates *et al.*, 2002; Gates, 2005; Decarreau *et al.*, 2008), but the nature of this contribution remains an open question.

For the spectra of nontronites with large $^{[4]}$Fe(III) contents, the δFe_2^{3+}–OH vibrations at 816 cm^{-1} broadened and decreased in intensity dramatically with the increase in $^{[4]}$Fe(III) content. Concomitantly, a distinct band at 763 cm^{-1} appeared. This new band at 763 cm^{-1} could not be interpreted as the δFe^{3+}Mg-OH vibration as previously observed for Fe(III)-montmorillonite (Petit *et al.*, 2002; Gaudin *et al.*, 2004, 2005) because no Mg was present in the samples. The 763 cm^{-1} band observed here appeared when the band at 816 cm^{-1} disappeared and was tentatively attributed to the δFe_2^{3+}-OH vibration in the case of large $^{[4]}$Fe(III) content. The νFe_2^{3+}-OH vibration at 3560 cm^{-1} did not vary for nontronites with large $^{[4]}$Fe(III) contents. A shoulder at 790 cm^{-1} was observed for samples with small $^{[4]}$Fe(III) contents. A band at

https://doi.org/10.1346/CCMN.2016.0640309 Published online by Cambridge University Press

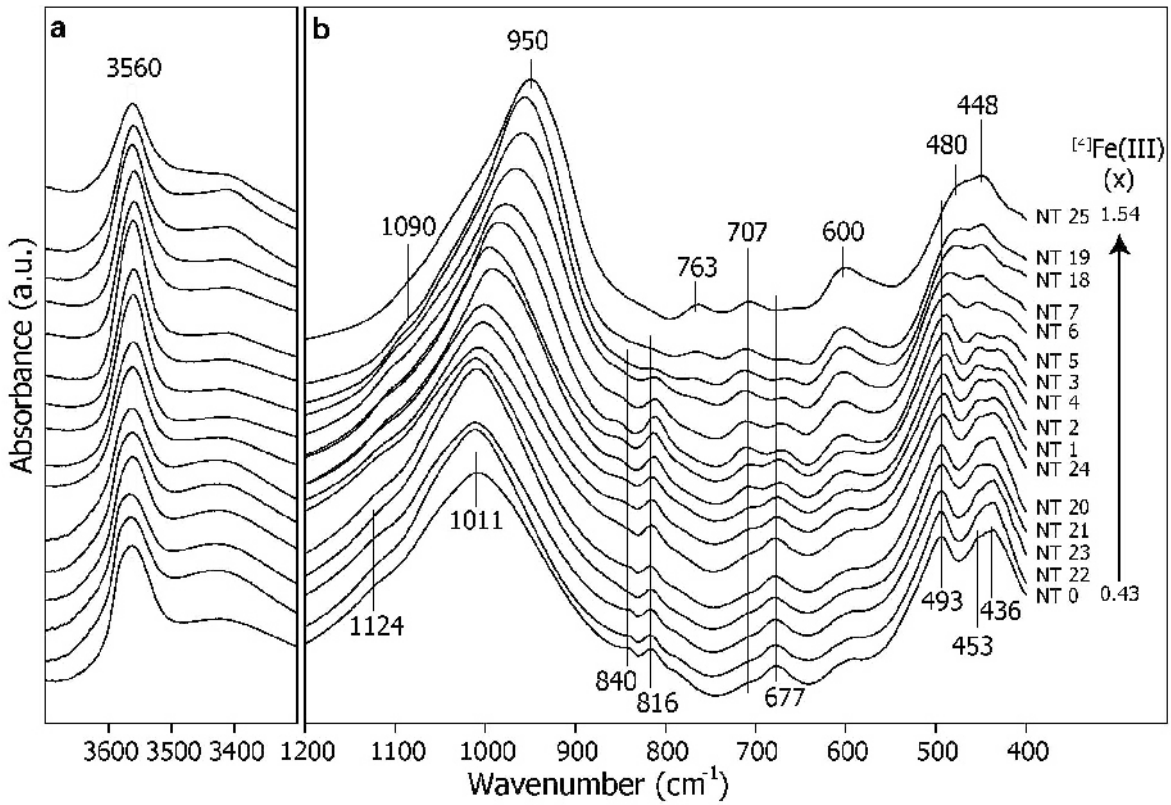

Figure 5. MIR spectra of the synthesized samples (NT25, NT19, NT18, NT7, NT6, NT5, NT3, NT4, NT2, NT1, NT24, NT20, NT21, NT23, NT22, and NT0) in the νOH region (a) and the 1200−400 cm^{-1} region (b). For both regions, the $^{[4]}$Fe(III) content (x) of the synthesized samples $[Si_{4-x}Fe(III)_x]Fe(III)_2O_{10}(OH)_2Na_x$ increases from the bottom to the top.

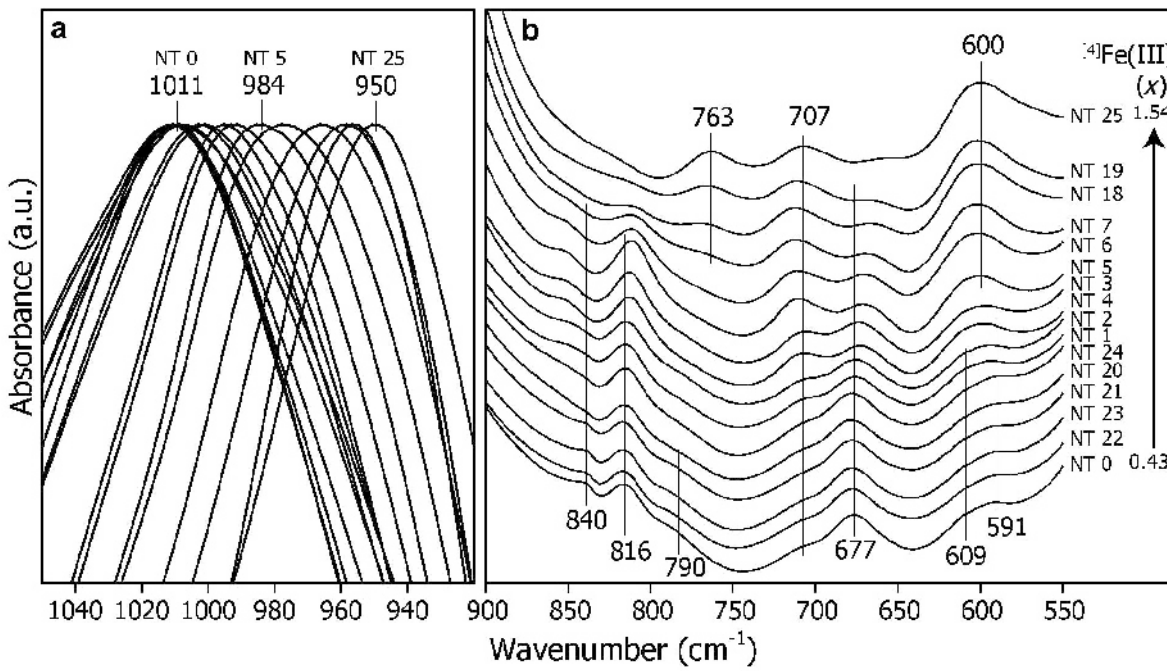

Figure 6. MIR spectra of the synthesized samples (NT25, NT19, NT18, NT7, NT6, NT5, NT3, NT4, NT2, NT1, NT24, NT20, NT21, NT23, NT22, and NT0) in the νSi−O region (a) and the 900−550 cm^{-1} region (b). For the 900−550 cm^{-1} region the $^{[4]}$Fe(III) content (x) of the synthesized samples $[Si_{4-x}Fe(III)_x]Fe(III)_2O_{10}(OH)_2Na_x$ increases from the bottom to the top.

https://doi.org/10.1346/CCMN.2016.0640309 Published online by Cambridge University Press

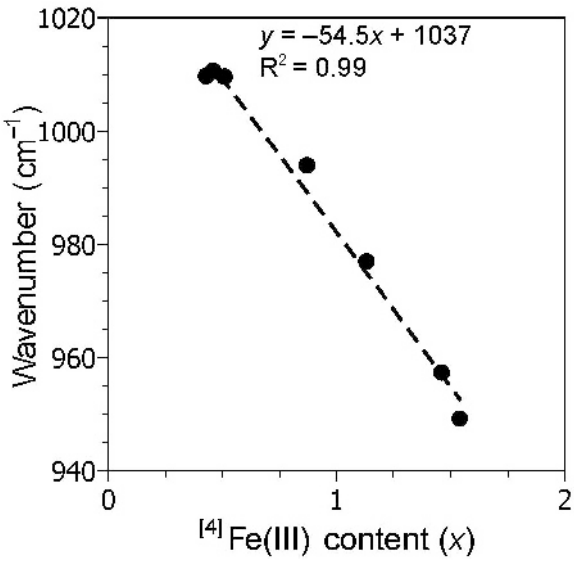

Figure 7. Correlation between the wavenumber (cm^{-1}) of the main νSi−O band and the $^{[4]}$Fe(III) content (x) of the synthesized samples $[Si_{4-x}Fe(III)_x]Fe(III)_2O_{10}(OH)_2M(I)_x$. The errors in the νSi−O wavenumber measurements and the estimation of the $^{[4]}$Fe(III) content (x) are indicated by the size of the symbol used.

790 cm^{-1} was often observed for natural nontronite and was usually attributed to the $\delta Fe^{3+}Mg^{2+}$−OH vibration (Goodman *et al.*, 1976; Grauby *et al.*, 1994; Keeling *et al.*, 2000; Gates, 2005) or to amorphous Si−O compounds (Manceau *et al.*, 2000a; Fialips *et al.*, 2002). The band at 790 cm^{-1} could not be attributed to $\delta Fe^{3+}Mg^{2+}$−OH vibrations here, however, because the syntheses were performed free of Mg. The nontronite samples synthesized did not contain enough, if any, amorphous Si-O compounds to explain the band at 790 cm^{-1}. This band belonged to nontronite, therefore, and might be attributed to a Si−O−Si symmetrical stretching vibration between two tetrahedrons, as observed by Farmer (1974) for other phyllosilicates.

750−400 cm^{-1} region. All nontronite spectra exhibited two bands at 707 cm^{-1} and 677 cm^{-1} (Figures 5b, 6b). The band at 677 cm^{-1} was attributed to the out-of-plane $^{[6]}Fe^{3+}$-O_{apical} vibration (*e.g.* Farmer, 1974; Goodman *et al.*, 1976; Gates, 2005; Petit *et al.*, 2015) and shifted toward lower wavenumber with an increase in the $^{[4]}$Fe(III) content. The band at 707 cm^{-1} increased in intensity, whereas the 677 cm^{-1} band decreased with the increase in the $^{[4]}$Fe(III) content. Decarreau *et al.* (2008) and Petit *et al.* (2015) attributed the band at 707 cm^{-1} to the $^{[4]}Fe^{3+}$−O vibration. The continuous increase in intensity of the bands at 707 cm^{-1} with the increase in the Fe(III)-for-Si(IV) substitutions provided evidence for this assignment.

All nontronite spectra had a broad complex band centered at ~600 cm^{-1} (Figure 6b). This band was at least partly attributed to the $^{[6]}Fe^{3+}-O_{apical}-Si^{4+}$ coupled lattice bending vibrations (Stubican and Roy, 1961; Gates, 2005; Petit *et al.*, 2015). Nevertheless, the intensity of this broad complex band increased with the $^{[4]}$Fe(III) content (Figure 6b), reflecting a possible contribution of $^{[4]}$Fe(III).

In the 550−400 cm^{-1} region (Figure 5), three bands at 493, 453, and 436 cm^{-1} could be observed for the nontronite sample with the lowest $^{[4]}$Fe(III) content, as for the natural nontronites (Goodman *et al.*, 1976; Gaudin *et al.*, 2004; Gates, 2005). The last band at 436 cm^{-1} disappeared progressively with the increase in the $^{[4]}$Fe(III) content. The two bands at 493 and 453 cm^{-1} were assigned to $Si^{4+}-O-^{[6]}Fe^{3+}$ vibrations (Gaudin *et al.*, 2004; Petit *et al.*, 2015). These bands shifted with an increase in $^{[4]}$Fe(III) content to 480 and 448 cm^{-1}, respectively.

Although MIR spectra varied dramatically along the series, the NIR spectra were similar for all synthetic nontronite samples (Figure 8).

Region of the first overtone of the OH-stretching vibrations. A band was observed at 6982 cm^{-1} (Figure 8) in all NIR spectra and corresponds to the first overtone of the νFe_2^{3+}-OH mode (Decarreau *et al.*, 2008; Madejová *et al.*, 2011; Petit *et al.*, 2015). The shoulder near 6800 cm^{-1} and the asymmetric absorption band at 5215 cm^{-1} were due to the water molecules in smectite (Cariati *et al.*, 1981, 1983a, 1983b). The intensities of the absorption bands linked to water molecules decreased significantly with an increase in the $^{[4]}$Fe(III) content, revealing a smaller water content in the highest-charged samples.

Combination vibrations region. In the combination vibrations region, a main absorption band at 4370 cm^{-1} was observed (Figure 8). This band was assigned to the combination between the ν and δ modes of the Fe_2^{3+}-OH groups (Gates, 2005; Decarreau *et al.*, 2008; Andrieux and Petit, 2010). Another band was observed at 4168 cm^{-1} and this could be assigned to the combination between the νFe_2^{3+}−OH band and the $^{[6]}Fe^{3+}-O_{apical}-Si^{4+}$ coupled lattice bending vibration (3559 + 609 = 4168 cm^{-1}; wavenumbers of the bands are obtained by the second derivative method; see the procedure developed by Baron and Petit, 2016).

DISCUSSION

Characterization of the nontronites synthesized

The data obtained from the HRTEM and XRD powder patterns indicated that the samples synthesized correspond to mono-mineral nontronites with a layered structure. The dioctahedral structure was confirmed in all synthetic samples by the FTIR spectra (only the vibration of Fe_2^{3+}-OH groups was observed). Chemical analyses performed on the solid phases (Table 2)

https://doi.org/10.1346/CCMN.2016.0640309 Published online by Cambridge University Press

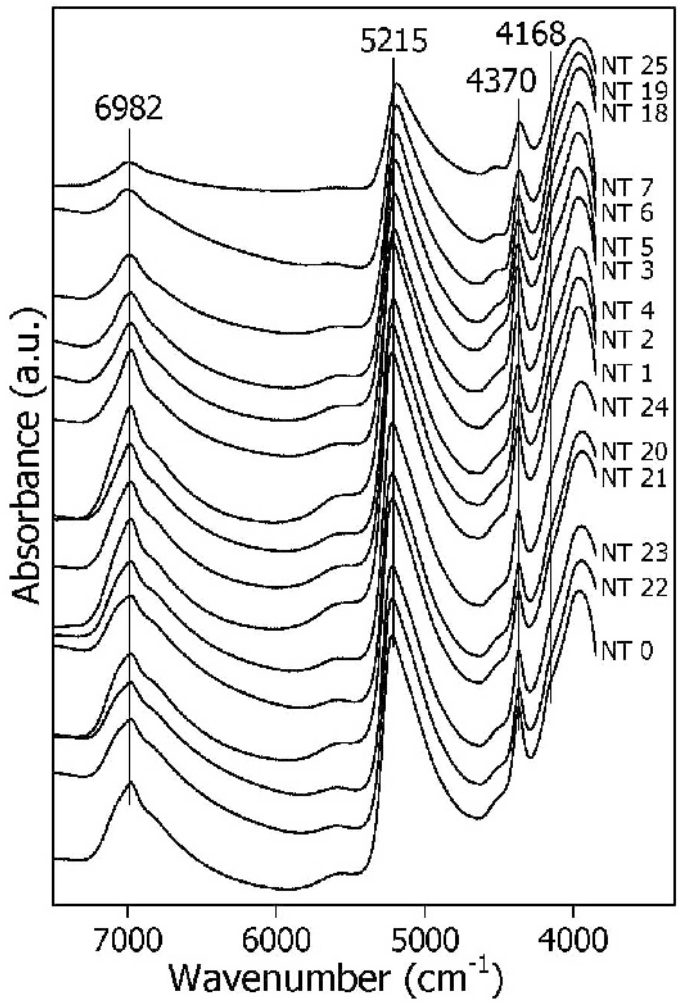

Figure 8. NIR spectra of the synthesized samples (NT25, NT19, NT18, NT7, NT6, NT5, NT3, NT4, NT2, NT1, NT24, NT20, NT21, NT23, NT22, and NT0). The $^{[4]}$Fe(III) content (x) of the synthesized samples $[Si_{4-x}Fe(III)_x]Fe(III)_2O_{10}(OH)_2Na_x$ increases from the bottom to the top.

revealed that the nontronite samples have an estimated layer charge (x) ranging from 0.43 to 1.54 per half-unit cell (Table 3). For most of the samples, the estimated $^{[4]}$Fe(III) content (x) from the half-unit cell was in good agreement with the charge calculated from the amount of interlayer cations. Nontronites with a layer charge (x) >0.6−0.7 per half-unit cell are uncommon in nature because of the more complex systems and generally neutral pH conditions (Decarreau *et al.*, 2008).

The increase in the $^{[4]}$Fe(III) content in the synthesized nontronites with synthesis pH was consistent with the progressive shift of the $d_{06\bar{3}3}$ (from 1.528 to 1.562 Å) and of the νSi-O vibration mode (from 1011 to 950 cm^{-1}). The data confirmed that the increase in layer charge (x) in the synthesized nontronite series was due to the increase in the Fe(III)-for-Si(IV) substitutions in the tetrahedral sheet. Furthermore, these synthetic nontronites exhibited various swelling behaviors after EG solvation, from smectitic swelling properties for the nontronites with the lowest tetrahedral charge to vermiculitic swelling behavior for the nontronites with the highest tetrahedral charge (charge per half-unit cell >0.8). Even for a layer charge (x) as high as 1.54, the swelling behavior is preserved. The evolution of the swelling behavior with the increase in layer charge is continuous along the synthetic nontronite series. This continuity in swelling behavior was observed previously by Suquet and Pezerat (1988) for a series of natural vermiculites with various charges. Note that for such series, the apparent discontinuity of the swelling properties sometimes observed depends more on the nature of the interlayer cations or solvation liquid than their layer charge.

Few spectroscopic methods are able to identify and quantify the $^{[4]}$Fe(III) content in smectites (Decarreau and Petit, 2014). Even for synthetic nontronite with an $^{[4]}$Fe(III) = 0.75 per half-unit cell, which corresponds to a high-charged smectite, Mössbauer or XANES spectro-

https://doi.org/10.1346/CCMN.2016.0640309 Published online by Cambridge University Press

scopies were not self-sufficient to quantify the $^{[4]}$Fe(III) content (Decarreau *et al.*, 2008). Using FTIR spectroscopy, one can estimate the $^{[4]}$Fe(III) content of the synthetic nontronite series from equation 2, through the shift of the νSi–O vibration from 1011 to 950 cm^{-1} (Figure 7). From the position of the νSi–O vibration, equation 2 allowed, therefore, the estimation of the tetrahedral charge of synthetic Fe(III)-rich dioctahedral smectites with a tetrahedral charge between 0.4 and 1.5 per half-unit cell due to Fe(III)-for-Si(IV) substitutions. Compared to the influence of the $^{[6]}$Fe(III) content on the wavenumber of the νSi–O band reported by Andrieux and Petit (2010) and Petit *et al.* (2015) for a chemical series of Al-Fe(III) smectites, the $^{[4]}$Fe(III) content influenced the νSi–O wavenumber five times more than the $^{[6]}$Fe(III) content (*i.e.* note the negative slope of −54.5 cm^{-1}/$^{[4]}$Fe(III) atoms for $^{[4]}$Fe(III) (Figure 7), instead of −9.5 cm^{-1}/$^{[6]}$Fe(III) atoms for $^{[6]}$Fe(III); Petit *et al.* (2015)). The increase in intensity of the $^{[4]}Fe^{3+}$–O band at ~707 cm^{-1}, as well as the shift of the Si^{4+}–O–$^{[6]}Fe^{3+}$ vibrations (from 493 and 453 to 480 and 448 cm^{-1}, respectively; Figure 6) with synthesis pH were also indicative of the $^{[4]}$Fe(III) content.

Lattice parameters

Tetrahedral Fe(III)-for-Si(IV) substitutions strongly affected the $d_{06\bar{3}3}$ value (Figure 9) and consequently the *b* parameter ($b = 6 \times d_{06\bar{3}3}$), as previously reported by Eggleton (1977); Brigatti (1983); Manceau *et al.* (2000b); Gaudin *et al.* (2004); Decarreau *et al.* (2008); and Petit *et al.* (2015). Nevertheless, the influence of the $^{[4]}$Fe(III) content on the $d_{06\bar{3}3}$ value was not continuous. For an $^{[4]}$Fe(III) content of >1.25 per half-unit cell in synthesized nontronites, the $d_{06\bar{3}3}$ values increase three times more than for an $^{[4]}$Fe(III) content of <1.25 (Figure 9). This change could originate from the changing environment around Si in the tetrahedral sheets (*i.e.* Si linked to three, two, or one $^{[4]}$Fe(III)).

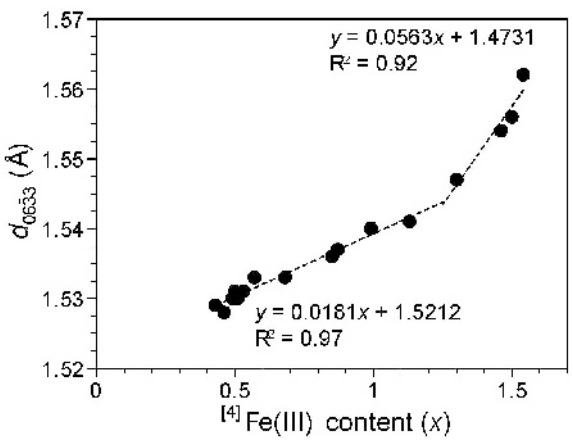

Figure 9. Correlation between the $^{[4]}$Fe(III) content (*x*) of the synthesized samples $[Si_{4-x}Fe(III)_x]Fe(III)_2O_{10}(OH)_2M(I)_x$ and the position of the $d_{06\bar{3}3}$. The error in the $d_{06\bar{3}3}$ measurements and the estimation of the $^{[4]}$Fe(III) content (*x*) are indicated by the size of the symbol used.

The role of pH during synthesis

All syntheses were performed from the same starting gel, which had an Fe/Si ratio of 0.74 (Table 1). The variable chemical parameters between the different syntheses were the pH_s and the Na content of the starting solution. The amount of Fe(III)-for-Si(IV) tetrahedral substitutions in the synthetic nontronites was approximately the same for a $pH_f < 11.8$ (± 0.2), whereas for a $pH_f > 11.8$ (± 0.2) the amount of $^{[4]}$Fe(III) content (*x*) increased with the increase in pH_f (Figure 10a).

An attempt was made to assess the link between the characteristics of the synthetic nontronite and the

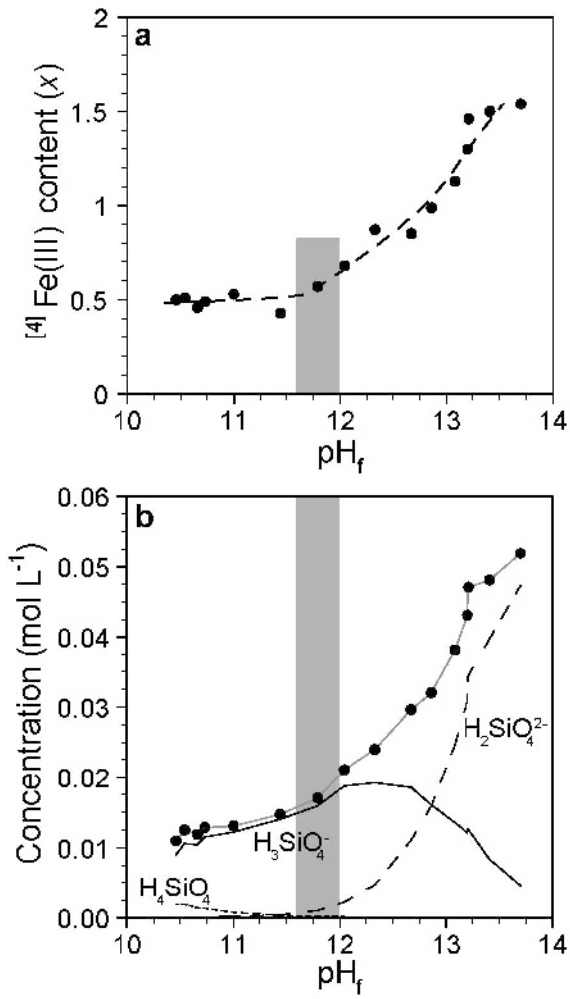

Figure 10. (a) Evolution of the $^{[4]}$Fe(III) content (*x*) per half-unit cell $[Si_{4-x}Fe(III)_x]Fe(III)_2O_{10}(OH)_2M(I)_x$ *vs.* pH at the end of the synthesis (pH_f) (Table 1). (b) Evolution of the concentrations of total aqueous Si and of the different Si species at the end of synthesis *vs.* pH_f. The shaded area corresponds to pH_f (11.8 ± 0.2) from which the $^{[4]}$Fe(III) content (*x*) increased with the increase in pH_f.

https://doi.org/10.1346/CCMN.2016.0640309 Published online by Cambridge University Press

chemical composition of the solution at the end of syntheses. The aqueous Si, Na, and Fe speciation calculations were performed using the *PHREEQC*® software associated with the *minteq*.v4 database (Parkhurst and Appelo, 2013). Calculations were performed using the pH_f and the measured total Na and Si aqueous concentrations (Table 1). For Fe, calculations were performed by considering the same value for all samples, and corresponded to the maximum concentration measured (*i.e.* 10^{-4} mol L^{-1}). Although the syntheses were performed at 150ºC, these calculations were conducted for a temperature of 25ºC for the following reasons: (1) due to the lack of precision concerning aqueous complexation constants at 150ºC for pH as high as 13−14, especially for aqueous Si species, and (2) because all measurements (aqueous and solid) were obtained at 25ºC. The main forms of aqueous Fe and Na in the solution at the end of syntheses were $Fe(OH)^-_{4(aq)}$ and $Na^+_{(aq)}$, respectively, which remained the same in the 10−14 pH_f range investigated. For Si, however, the aqueous speciation depended heavily on pH (Figure 10b). The main predicted species were $H_3SiO^-_{4(aq)}$ and $H_2SiO^-_{4(aq)}$, and the predicted concentration of the $H_2SiO^-_{4(aq)}$ species increased greatly with an increase in pH_f (Figure 10b). For $pH_f < 11.8$ (±0.2), the total aqueous Si concentration remained approximately constant, and the main predicted form was $H_3SiO^-_{4(aq)}$. These results were correlated with the relatively constant values of $^{[4]}$Fe(III) measured for the synthesized nontronites obtained at $pH_f < 11.8$ (± 0.2) (Figure 10b). For $pH_f > 11.8$ (± 0.2), total aqueous Si concentration as well as that of $H_2SiO^-_{4(aq)}$ species increased with increasing pH_f. These changes in Si speciation were correlated with the increase in the $^{[4]}$Fe(III) content in synthesized nontronites (Figure 10a). An increase in the proportion of aqueous anionic Si species (*i.e.* $H_3SiO^-_{4(aq)}$ and $H_2SiO^-_{4(aq)}$) induced an increase in the solubility of pure crystalline Si phases (Iler, 1979). Both $H_3SiO^-_{4(aq)}$ and $H_2SiO^-_{4(aq)}$ act, therefore, as inhibitors during precipitation of pure crystalline Si phases. For the Si/Fe(III) system, the presence of a significant proportion of $H_3SiO^-_{4(aq)}$ or $H_2SiO^-_{4(aq)}$ could be the origin of the decrease in the Si content in the tetrahedral sheet of the synthesized nontronites with the increase in pH_f. Consequently, both $H_3SiO^-_{4(aq)}$ and $H_2SiO^-_{4(aq)}$ could promote the presence of Fe(III) in tetrahedral coordination in synthesized nontronites. A similar observation was reported by Pokrovski *et al.* (2003) for the structure of Si/Fe(III) aqueous complexes studied using XANES and EXAFS spectroscopic methods. At pH = 3 and for total aqueous Si concentrations of 0.05 mol L^{-1} and 0.16 mol L^{-1}, those authors reported that although the main coordination of Fe(III) in Si/Fe(III) aqueous complexes was octahedral for both total aqueous Si concentrations, a significant amount of Fe(III) was also present in tetrahedral coordination for the largest total aqueous Si concentration investigated. A similar effect of the total aqueous Si concentration on the amount of $^{[4]}$Fe(III) was observed for the synthesis of nontronites with the increase in pH_f (see Figure 10). The increase in the proportion of $H_3SiO^-_{4(aq)}$ and $H_2SiO^-_{4(aq)}$ with pH_f favored, therefore, the tetrahedral coordination of Fe(III) in the synthesized nontronites.

CONCLUSIONS

The present study has shown that the crystal chemistry of the Fe(III)-nontronites depended heavily on the amount of $H_3SiO^-_{4(aq)}$ and $H_2SiO^-_{4(aq)}$ species during nontronite formation. A series of Fe(III)-nontronites was synthesized with various amounts of tetrahedral Fe(III)-for-Si(IV) substitutions to assess the link between the chemical speciation of crystallization fluids and the crystal-chemistry of the Fe(III)-nontronites. The range of tetrahedral charges (x) measured for this synthetic Fe(III)-nontronite series was from 0.43 to as high as 1.54 per half-unit cell ($[Si_{4-x}Fe(III)_x]Fe(III)_2O_{10}(OH)_2Na_x$).

The aqueous Si speciation, which is pH dependent, controlled the amount of tetrahedral Fe(III)-for-Si(IV) substitutions in synthetic nontronites. Because the formation of nontronites with very large $^{[4]}$Fe(III) contents (>0.7 per half-unit cell) required a basic pH and an Al-poor medium, such very high-charged nontronite is unusual in natural environments. Indeed, if Al is present in crystallization fluids, the strong preference of Al(III)-for-Si(IV) compared to Fe(III)-for-Si(IV) substitutions in tetrahedral sheets favors $^{[4]}$Al(III) (Decarreau and Petit, 2014).

This series was valuable because the tetrahedral charge was the only variable parameter, and exhibited a wide range of $^{[4]}$Fe(III) values. This series of Fe(III)-nontronites could be used as a reference, therefore, for quantification of the $^{[4]}$Fe(III) content in phyllosilicates to evaluate the capability of spectroscopic methods or for calibration. Finally, even though the redox reactivity of smectites is known to be sensitive to the crystal-chemistry of smectites, which determines the number and activity of Fe(II) sites (Neumann *et al.*, 2008, 2009, 2011), the specific role played by the $^{[4]}$Fe(III) in electron transfer is unknown (see review by Stucki, 2013). The use of the Fe(III)-nontronite series could be of great interest in understanding the role played by $^{[4]}$Fe(III) on the redox properties of these materials, in particular in processes implying chemical and/or microbial reduction studies.

ACKNOWLEDGMENTS

The authors are grateful to J. Rousseau for her technical help during TEM preparations and observations. They also thank L. Dzene for technical help during the AA measurements. One of the authors, F.B., acknowledges The Clay Minerals Society for a student travel grant, which allowed him to present these results at the Euroclay 2015 meeting, Edinburgh, UK. Editor-in-Chief, J.W. Stucki, Associate-Editor, A. Thompson, and three anonymous reviewers are acknowledged for their constructive reviews.

REFERENCES

Andrieux, P. and Petit, S. (2010) Hydrothermal synthesis of dioctahedral smectites: The Al–Fe^{3+} chemical series: Part I: Influence of experimental conditions. *Applied Clay Science*, **48**, 5–17.

Baron, F. and Petit, S. (2016) Interpretation of the infrared spectra of the lizardite–nepouite series in the near- and mid-infrared range. *American Mineralogist*, **101**, 423–430.

Brigatti, M.F. (1983) Relationships between composition and structure in Fe-rich smectites. *Clay Minerals*, **18**, 177–186.

Brindley, G.W. (1966) Ethylene glycol and glycerol complexes of smectites and vermiculites. *Clay Minerals*, **6**, 237–259.

Brindley, G.W. and Brown, G. (1980) *Crystal Structures of Clay Minerals and their X-ray Identification*. Mineralogical Society, London.

Cariati, F., Erre, L., Micera, G., Piu, P., and Gessa, C. (1983a) Effects of layer charge on the near-infrared spectra of water molecules in smectites and vermiculites. *Clays and Clay Minerals*, **31**, 447–449.

Cariati, F., Erre, L., Micera, G., Piu, P., and Gessa, C. (1983b) Polarization of water molecules in phyllosilicates in relation to exchange cations as studied by near infrared spectroscopy. *Clays and Clay Minerals*, **31**, 155–157.

Cariati, F., Erre, L., Micera, G., Piu, P., and Gessa, C. (1981) Water molecules and hydroxyl groups in montmorillonites as studied by near infrared spectroscopy. *Clays and Clay Minerals*, **29**, 157–159.

Chassin, P. (1972) Étude de la conformation de la molécule d'éthane 1-2 diol adsorbée sur les phyllites 2-1. *Bulletin du Groupe Français des Argiles*, **24**, 79–88.

Decarreau, A. and Petit, S. (2014) Fe^{3+}/Al^{3+} partitioning between tetrahedral and octahedral sites in dioctahedral smectites. *Clay Minerals*, **49**, 657–665.

Decarreau, A., Petit, S., Vieillard, P., and Dabert, N. (2004) Hydrothermal synthesis of aegirine at 200ºC. *European Journal of Mineralogy*, **16**, 85–90.

Decarreau, A., Petit, S., Martin, F., Farges, F., Vieillard, P., and Joussein, E. (2008) Hydrothermal synthesis, between 75 and 150ºC, of high-charge, ferric nontronites. *Clays and Clay Minerals*, **56**, 322–337.

Eggleton, R.A. (1977) Nontronite: Chemistry and X-ray diffraction. *Clay Minerals*, **12**, 181–194.

Farmer, V.C. (1974) *The Infrared Spectra of Minerals*. Monograph **5**, The Mineralogical Society, London.

Ferrage, E., Lanson, B., Sakharov, B.A., Geoffroy, N., Jacquot, E., and Drits, V.A. (2007) Investigation of dioctahedral smectite hydration properties by modeling of X-ray diffraction profiles: Influence of layer charge and charge location. *American Mineralogist*, **92**, 1731–1743.

Ferrage, E., Lanson, B., Michot, L.J., and Robert, J.-L. (2010) Hydration properties and interlayer organization of water and ions in synthetic Na-smectite with tetrahedral layer charge. Part 1. Results from X-ray diffraction profile modeling. *The Journal of Physical Chemistry C*, **114**, 4515–4526.

Fialips, C.-I., Huo, D., Yan, L., Wu, J., and Stucki, J.W. (2002) Effect of Fe oxidation state on the IR spectra of Garfield nontronite. *American Mineralogist*, **87**, 630–641.

Gates, W.P. (2005) Infrared spectroscopy and the chemistry of dioctahedral smectites. Pp. 125–168 in: *The Application of Vibrational Spectroscopy to Clay Minerals and Layered Double Hydroxides* (J. Theo Kloprogge, editor). The Clay Minerals Society, Aurora, Colorado, USA.

Gates, W.P. (2008) Cation mass-valence sum (CM-VS) approach to assigning OH-bending bands in dioctahedral smectites. *Clays and Clay Minerals*, **56**, 10–22.

Gates, W.P., Slade, P.G., Manceau, A., and Lanson, B. (2002) Site occupancies by iron in nontronites. *Clays and Clay Minerals*, **50**, 223–239.

Gaudin, A., Buatier, M.D., Beaufort, D., Petit, S., Grauby, O., and Decarreau, A. (2005) Characterization and origin of Fe^{3+}-montmorillonite in deep-water calcareous sediments (Pacific Ocean, Costa Rica margin). *Clays and Clay Minerals*, **53**, 452–465.

Gaudin, A., Petit, S., Rose, J., Martin, F., Decarreau, A., Noack, Y., and Borschneck, D. (2004) The accurate crystal chemistry of ferric smectites from the lateritic nickel ore of Murrin Murrin (Western Australia). II. Spectroscopic (IR and EXAFS) approaches. *Clay Minerals*, **39**, 453–467.

Goodman, B.A., Russell, J.D., Fraser, A.R., and Woodhams, F.W.D. (1976) A Mössbauer and I.R. spectroscopic study of the structure of nontronite. *Clays and Clay Minerals*, **24**, 53–59.

Grauby, O., Petit, S., Decarreau, A., and Baronnet, A. (1994) The nontronite–saponite series; an experimental approach. *European Journal of Mineralogy*, **6**, 99–112.

Gupta, V.K., Mohan, D., and Saini, V.K. (2006) Studies on the interaction of some azo dyes (naphthol red-J and direct orange) with nontronite mineral. *Journal of Colloid and Interface Science*, **298**, 79–86.

Heuser, M., Andrieux, P., Petit, S., and Stanjek, H. (2013) Iron-bearing smectites: a revised relationship between structural Fe, b cell edge lengths and refractive indices. *Clay Minerals*, **48**, 97–103.

Hofstetter, T.B., Neumann, A., and Schwarzenbach, R.P. (2006) Reduction of nitroaromatic compounds by Fe(II) species associated with iron-rich smectites. *Environmental Science & Technology*, **40**, 235–242.

Iler, R.K. (1979) *The Chemistry of Silica: Solubility, Polymerization, Colloid and Surface Properties and Biochemistry of Silica*. Wiley, New York.

Ilgen, A.G., Foster, A.L., and Trainor, T.P. (2012) Role of structural Fe in nontronite NAu-1 and dissolved Fe(II) in redox transformations of arsenic and antimony. *Geochimica et Cosmochimica Acta*, **94**, 128–145.

Jaisi, D.P., Dong, H., Plymale, A.E., Fredrickson, J.K., Zachara, J.M., Heald, S., and Liu, C. (2009) Reduction and long-term immobilization of technetium by Fe(II) associated with clay mineral nontronite. *Chemical Geology*, **264**, 127–138.

Keeling, J.L., Raven, M.D., and Gates, W.P. (2000) Geology and characterization of two hydrothermal nontronites from weathered metamorphic rocks at the Uley graphite mine, South Australia. *Clays and Clay Minerals*, **48**, 537–548.

Köster, H.M., Ehrlicher, U., Gilg, H.A., Jordan, R., Murad, E., and Onnich, K. (1999) Mineralogical and chemical characteristics of five nontronites and Fe-rich smectites. *Clay Minerals*, **34**, 579–599.

Li, H., Li, Y., Xiang, L., Huang, Q., Qiu, J., Zhang, H., Sivaiah, M.V., Baron, F., Barrault, J., Petit, S., and Valange, S. (2015) Heterogeneous photo-Fenton decolorization of Orange II over Al-pillared Fe-smectite: Response surface approach, degradation pathway, and toxicity evaluation. *Journal of Hazardous Materials*, **287**, 32–41.

Liu, R., Xiao, D., Guo, Y., Wang, Z., and Liu, J. (2014) A novel photosensitized Fenton reaction catalyzed by sandwiched iron in synthetic nontronite. *RSC Advances*, **4**, 12958–12963.

MacEwan, D.M.C. (1948) Complexes of clays with organic compounds. I. Complex formation between montmorillonite and halloysite and certain organic liquids. *Transactions of the Faraday Society*, **44**, 349–367.

Madejová, J., Bujdak, J., Gates, W.P., and Komadel, P. (1996) Preparation and infrared spectroscopic characterization of reduced-charge montmorillonite with various Li contents. *Clay Minerals*, **31**, 233–241.

Madejová, J., Balan, E., and Petit, S. (2011) Application of

vibrational spectroscopy to the characterization of phyllosilicates and other industrial minerals. Pp. 171–226 in: *Advances in the Characterization of Industrial Minerals* (G.E. Christidis, editor). EMU Notes in Mineralogy, **9**, European Mineralogical Union and the Mineralogical Society of Great Britain & Ireland.

Manceau, A., Drits, V.A., Lanson, B., Chateigner, D., Wu, J., Huo, D., Gates, W.P., and Stucki, J.W. (2000a) Oxidation-reduction mechanism of iron in dioctahedral smectites: II. Crystal chemistry of reduced Garfield nontronite. *American Mineralogist*, **85**, 153–172.

Manceau, A., Lanson, B., Drits, V.A., Chateigner, D., Gates, W.P., Wu, J., Huo, D., and Stucki, J.W. (2000b) Oxidation-reduction mechanism of iron in dioctahedral smectites: I. Crystal chemistry of oxidized reference nontronites. *American Mineralogist*, **85**, 133–152.

Michot, L.J., Bihannic, I., Pelletier, M., Rinnert, E., and Robert, J.L. (2005) Hydration and swelling of synthetic Na-saponites: Influence of layer charge. *American Mineralogist*, **90**, 166–172.

Neumann, A., Hofstetter, T.B., Lüssi, M., Cirpka, O.A., Petit, S., and Schwarzenbach, R.P. (2008) Assessing the redox reactivity of structural iron in smectites using nitroaromatic compounds as kinetic probes. *Environmental Science & Technology*, **42**, 8381–8387.

Neumann, A., Hofstetter, T.B., Skarpeli-Liati, M., and Schwarzenbach, R.P. (2009) Reduction of polychlorinated ethanes and carbon tetrachloride by structural Fe(II) in smectites. *Environmental Science & Technology*, **43**, 4082–4089.

Neumann, A., Petit, S., and Hofstetter, T.B. (2011) Evaluation of redox-active iron sites in smectites using middle and near infrared spectroscopy. *Geochimica et Cosmochimica Acta*, **75**, 2336–2355.

Parkhurst, D.L. and Appelo, C.A.J. (2013) Description of input and examples for PHREEQC version 3 – A computer program for speciation, batch-reaction, one-dimensional transport, and inverse geochemical calculations. *U.S. Geological Survey Techniques and Methods*, available at http://pubs.usgs.gov/tm/06/a43/.

Petit, S., Prot, T., Decarreau, A., Mosser, C., and Toledo-Groke, M.C. (1992) Crystallochemical study of a population of particles in smectites from a lateritic weathering profile. *Clays and Clay Minerals*, **40**, 436–445.

Petit, S., Robert, J.-L., Decarreau, A., Besson, G., Grauby, O., and Martin, F. (1995) Apport des méthodes spectroscopiques à la caractérisation des phyllosilicates 2:1. *Bulletin des Centres de Recherches Exploration-Production Elf Aquitaine*, **19**, 119–147.

Petit, S., Caillaud, J., Righi, D., Madejová, J., Elsass, F., and Köster, H.M. (2002) Characterization and crystal chemistry of an Fe-rich montmorillonite from Ölberg, Germany. *Clay Minerals*, **37**, 283–297.

Petit, S., Decarreau, A., Gates, W., Andrieux, P., and Grauby, O. (2015) Hydrothermal synthesis of dioctahedral smectites: The Al–Fe^{3+} chemical series. Part II: Crystal-chemistry. *Applied Clay Science*, **104**, 96–105.

Pokrovski, G.S., Schott, J., Farges, F., and Hazemann, J.-L. (2003) Iron (III)-silica interactions in aqueous solution: insights from X-ray absorption fine structure spectroscopy. *Geochimica et Cosmochimica Acta*, **67**, 3559–3573.

Poulet, F., Bibring, J.-P., Mustard, J.F., Gendrin, A., Mangold, N., Langevin, Y., Arvidson, R.E., Gondet, B., and Gomez, C. (2005) Phyllosilicates on Mars and implications for early Martian climate. *Nature*, **438**, 623–627.

Poulet, F., Beaty, D.W., Bibring, J.-P., Bish, D., Bishop, J.L., Noe Dobrea, E., Mustard, J.F., Petit, S., and Roach, L.H. (2009) Key scientific questions and key investigations from the first international conference on Martian phyllosilicates. *Astrobiology*, **9**, 257–267.

Reynolds, R.C. (1965) An X-ray study of an ethylene-glycol montmorillonite complex. *American Mineralogist*, **50**, 990–1001.

Sato, T., Watanabe, T., and Otsuka, R. (1992) Effects of layer charge, charge location, and energy change on expansion properties of dioctahedral smectites. *Clays and Clay Minerals*, **40**, 103–113.

Strickland, J.D.H. and Parsons, T.R. (1972) *A Practical Handbook of Seawater Analysis.* Fisheries Research Board of Canada, Ottawa.

Stubican, V. and Roy, R. (1961) Isomorphous substitution and infra-red spectra of the layer lattice silicates. *American Mineralogist*, **46**, 32–51.

Stucki, J.W. (2013) Properties and behaviour of iron in clay minerals. Pp. 559–612 in: *Handbook of Clay Science* (F. Bergaya and G. Lagaly, editors). 2nd edition, Elsevier, Amsterdam.

Suquet, H. and Pezerat, H. (1988) Comments on the classification of trioctahedral 2:1 phyllosilicates. *Clays and Clay Minerals*, **36**, 184–186.

Suquet, H., Iiyama, J.T., Kodama, H., and Pezerat, H. (1977) Synthesis and swelling properties of saponites with increasing layer charge. *Clays and Clay Minerals*, **25**, 231–242.

Suquet, H., Malard, C., and Pezerat, H. (1987) Structure et propriétés d'hydratation des nontronites. *Clay Minerals*, **22**, 157–167.

Yan, L. and Stucki, J.W. (1999) Effects of structural Fe oxidation state on the coupling of interlayer water and structural Si-O stretching vibrations in montmorillonite. *Langmuir*, **15**, 4648–4657.

Yan, L. and Stucki, J.W. (2000) Structural perturbations in the solid–water interface of redox transformed nontronite. *Journal of Colloid and Interface Science*, **225**, 429–439.

Yang, J., Kukkadapu, R.K., Dong, H., Shelobolina, E.S., Zhang, J., and Kim, J. (2012) Effects of redox cycling of iron in nontronite on reduction of technetium. *Chemical Geology*, **291**, 206–216.

Zen, J.M., Jeng, S.H., and Chen, H.J. (1996) Catalysis of the electroreduction of hydrogen peroxide by nontronite clay coatings on glassy carbon electrodes. *Journal of Electroanalytical Chemistry*, **408**, 157–163.

(*Received 27 October 2015; revised 29 June 2016; Ms. 1058; AE: A. Thompson*)